

FULL PAPER

Open Access



Ambient noise tomography for a high-resolution 3D S-wave velocity model of the Kinki Region, Southwestern Japan, using dense seismic array data

Bokani Nthaba^{1,2}, Tatsunori Ikeda^{1,3}, Hiro Nimiya^{1,4}, Takeshi Tsuji^{1,3,5*}  and Yoshihisa Iio⁶

Abstract

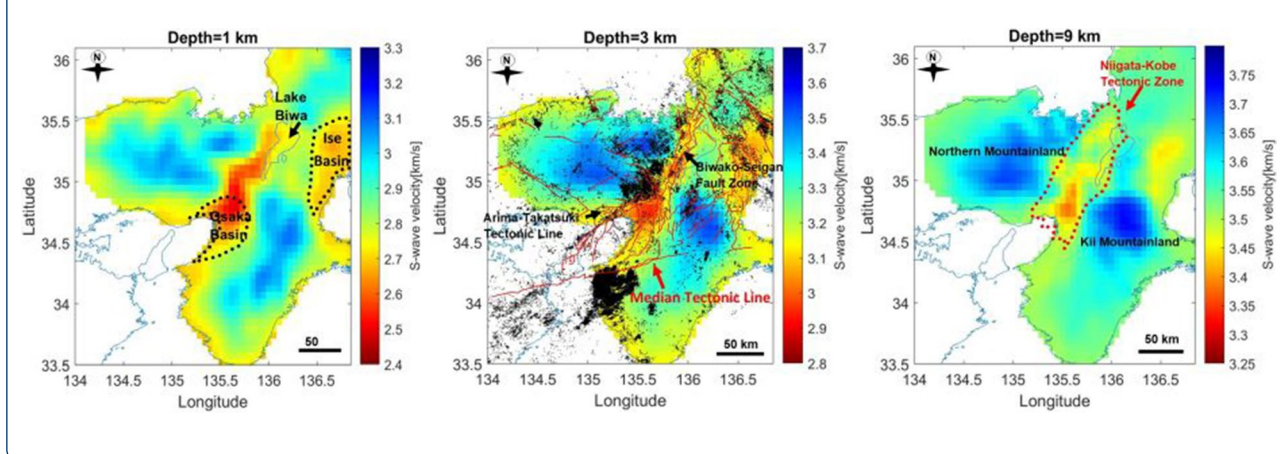
Research interest in the Kinki region, southwestern Japan, has been aroused by the frequent occurrence of micro-earthquake activity that do not always coincide with documented active fault locations. Previous studies in the Kinki region focused mainly on deep, large-scale structures and could not efficiently resolve fine-scale (~ 10 km) shallow crustal structures. Hence, characterization of the upper crustal structure of this region at an improved spatial resolution is required. From the cross-correlation of the vertical components of the ambient seismic noise data recorded by a densely distributed seismic array, we estimated Rayleigh wave phase velocities using a frequency domain method. Then, we applied a direct surface wave tomographic method for the measured phase velocity dispersion data to obtain a 3D S-wave velocity model of the Kinki region. The estimated velocity model reveals a NE–SW trending low-velocity structure coinciding with the Niigata–Kobe Tectonic Zone (NKTZ) and the active Biwako-seigan Fault Zone (BSFZ). Also, we identified fine-scale low-velocity structures coinciding with known active faults on the eastern side of the NKTZ, as well as sets of low-velocity structures across the Tanba region. Furthermore, sedimentary basins manifest as low-velocity zones extending to depths ranging from ~ 1.5 to 2 km, correlating with those reported in previous studies. Our results therefore contribute towards fundamental understanding of earthquake faulting as well as tectonic boundary and will be useful for hazard assessment and disaster mitigation.

Keywords: Ambient noise tomography, S-wave velocity model, Niigata–Kobe Tectonic Zone, Kinki region, Zero-crossing method, Surface waves

*Correspondence: tsuji@syst.u-tokyo.ac.jp

⁵ Department of Systems Innovation, Faculty of Engineering, The University of Tokyo, Tokyo 113-8656, Japan
Full list of author information is available at the end of the article

Graphical abstract



Introduction

To unravel heterogeneities within the crustal structure and upper mantle over a wide area, very few geophysical techniques with proven efficacy are available (Suemoto et al. 2020). Active-source geophysical techniques such as seismic reflection and refraction can be used to map and characterize geological structures at high resolution. A striking example is a study by Sato et al. (2009), in which deep seismic reflection profiling was employed to reveal several active reverse faults along a 135-km-long Osaka–Suzuka seismic profile. Likewise, Ito et al. (2006) conducted a similar survey along the N–S-trending Shingu–Maizuru line. However, this approach only provides details about fault locations and geologic boundaries along the profiles, and heterogeneities across the profiles can only be established from multiple profiles. Therefore, this approach is not well suited to constructing large-scale geological models for areas as large as the Kinki region.

Conversely, P- and S-wave travel-time tomography utilizing earthquake data over a wide area has provided significant results, resolving major structures such as faults and geologic boundaries (Kato et al. 2009, 2021; Matsubara et al. 2008; Nakajima et al. 2009; Yolsal-Cevikbilen et al. 2012). Even so, the downside of this approach is that the resolution of geological structures depends on the distribution of natural earthquakes (Suemoto et al. 2020). Using teleseismic data, surface wave tomography can also be applied. However, due to the occurrence of attenuation and scattering as distant waves propagate, teleseismic propagation paths complicate short-period (< 20 s) measurements (Bensen et al. 2007; Yang 2014). Such short-period measurements are the core of our objectives in this study as we seek to resolve shallow crustal features within the Kinki region.

The emergence of ambient noise tomography (ANT) in recent years has transformed seismic tomography because it can circumvent the shortcomings of traditional earthquake surface wave tomography (Sabra et al. 2005; Shapiro et al. 2005). The ANT method utilizes ambient noise to extract surface wave Green's functions between pairs of seismic stations by cross-correlating continuous seismic waveforms recorded at those stations (Shapiro et al. 2005; Weaver and Lobkis 2004). In this method, surface wave dispersion data between pairs of seismic stations can be estimated in the absence of earthquakes because each station can operate as a virtual source and a receiver (Shapiro et al. 2005; Weaver and Lobkis 2004). Since the inception and further developments of permanent and temporary high-quality seismic networks, ANT has been successfully utilized to delineate subsurface geologic features in various geological settings (Chen et al. 2018; Lin et al. 2008; Nishida et al. 2008; Shapiro et al. 2005). Suemoto et al. (2020) applied ambient noise surface wave tomography to estimate a high-resolution 3D S-wave velocity structure of the San-in area using continuously recorded seismic waveforms by a seismic network comprising Hi-net stations (Obara et al. 2005) and the Manten project array (Iio et al. 2018). Similarly, Nimiya et al. (2020) successfully utilized continuously recorded ambient noise data by Hi-net stations to construct the 3D S-wave velocity model of central Japan.

Numerous destructive earthquakes have occurred in the Kinki region (Hyodo and Hirahara 2003; Usami 2003), particularly in the western side of the Kinki triangle (Tanba region; Wakita 2013), bounded by the ENE–WSW strike-slip Arima–Takatsuki Tectonic Line (ATTL) to the south (Hallo et al. 2019; Iio 1996; Katao et al. 1997; Matsushita and Imanishi 2015) and the reactivated Niigata–Kobe Tectonic Zone (NKTZ)

to the east (Sagiya et al. 2000). Additionally, there is an inconsistency between the hypocenters of micro-earthquake events recorded across the entire Tanba region and the location of documented faults (Kato and Ueda 2019). Some of these events are linearly distributed between pairs of known faults, or in the same direction as known faults (Oike 1976). The chain of seismic alignment between pairs of known faults suggests the possible existence of concealed active faults in those areas, or continuity of known fault systems. Therefore, constructing a high-resolution 3D S-wave velocity structure of the Kinki region contribute to investigating the possible existence of undocumented fault zones in areas characterized by aligned distribution of earthquake hypocenters.

Previous seismic studies in the Kinki region (e.g., Nishida et al. 2008) focused mainly on deep, large-scale structures and could not efficiently resolve fine-scale (~10 km) shallow crustal structures and sharp geological boundaries. As such, we applied ambient noise tomographic inversion to provide an improved constraint on shallow-crustal structures and geological boundaries in the Kinki region using data recorded by the densely distributed permanent and temporary seismic stations.

Geologic setting

In the Kinki region, southwestern Japan, the Eurasian (EUR) plate overrides the subducting Philippine Sea (PHS) oceanic plate (Aoki et al. 2016). The southeastward movement of the incipient Amurian plate (Amur Plate) with respect to the EUR plate and a shift in the subduction direction of the PHS plate (Taira 2001) has generated relatively new, large fault zones or continually reactivates the old ones, a process referred to as neotectonics (Barnes 2008).

The major contributors in neotectonics faulting in the Kinki region comprise, among others, the reactivated Median Tectonic Line (MTL; black line in Fig. 1a), which has a right-lateral strike-slip fault movement (Barnes 2008). The MTL divides the Kinki region into outer zone and inner zone (Matsushita 1963). On the one hand, the outer zone is characterized by four zonally arranged terrains from north to south: namely, the Sanbagawa metamorphic terrain, Chichibu terrain, Hidaka terrain, and Muro terrain (SMZ, CT, HT, and MT; Fig. 1a). On the other hand, the zonal arrangement of geologic formations in the inner zone is not prominent, and it is characterized by the Neogene volcanic and sedimentary series of the Tango-Tajima terrain (TTT), the Yakuno intrusive rocks and marine formations of the Maizuru zone (MZ),

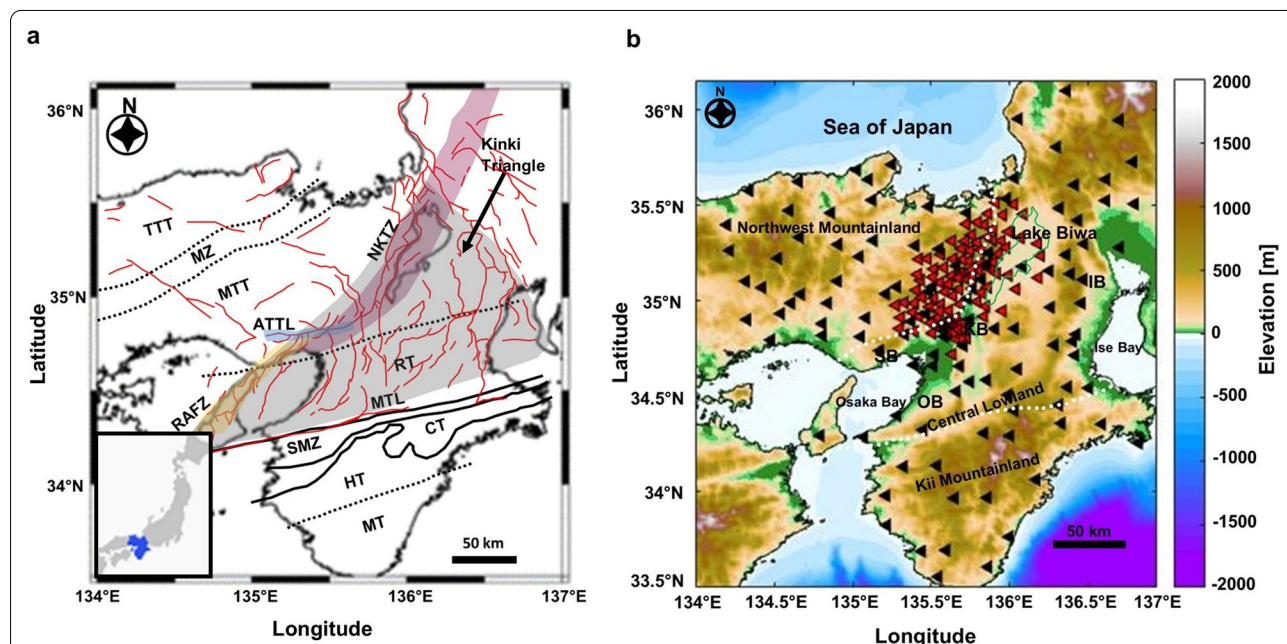


Fig. 1 **a** Map of the Kinki region showing the spatial distribution of tectonic structures. Red lines represent active faults (GSJ-AIST 2021), thick purple, yellow, and light blue lines represent the Niigata-Kobe Tectonic Zone (NKTZ), Rokko Active Fault Zone (RAFZ), and the Arima-Takatsuki Tectonic Line (ATTL), respectively. Also shown are the locations of the Median Tectonic Line (MTL), and tectonic divisions of the Kinki region, comprising Tango-Tajima Terrain (TTT), Maizuru Zone (MZ), Mino-Tamba Terrain (MTT), Ryoke Terrain (RT), Sanbagawa Metamorphic Zone (SMZ), Chichibu Terrain (CT), Hidaka Terrain (HT), and Muro Terrain (MT). The insert shows the location of the Kinki region within Japan. **b** Topographic map of the Kinki region. Black and red triangles indicate the locations of permanent and temporary stations, respectively. White, broken lines indicate the boundaries between the Northwestern Mountainland, Central Lowland, and Kii Mountainland

Cretaceous granites of the Mino-Tanba terrain (MTT), and metamorphic and granitic rocks of the Ryoke terrain (RT; Fig. 1a) (Matsushita 1963).

Huzita (1980) delineated a triangular-shaped neotectonics zone characterized by the E–W compression in the upper crust and undulating topography of alternating sedimentary basins and mountain ranges, called the Kinki triangle (gray-shaded area in Fig. 1a). This tectonic zone provided Kinki region with its civilizational homelands, including the Osaka, Nara, Kyoto and Ise basins (Barnes 2008). The Kinki triangle is characterized by numerous Quaternary active faults predominantly oriented in the N–S direction and some NE–SW or NW–SE strike–slip faults (Research Group for Active Faults of Japan 1991).

Around the Osaka area, numerous strike–slip and reverse active faults of diverse orientations exist (Research Group for Active Faults of Japan 1991). The significance of these faults was highlighted by the highly catastrophic 1995 M_w 7.2 Kobe earthquake, which resulted from the strike–slip displacements on the Rokko-Active Fault Zone (Kanamori 1995; Katao et al. 1997). In addition, a shallow crustal earthquake of M_w 5.6 occurred in 2018, proximal to the zone of intersection between the ATTL, the Uemachi and Ikoma fault zones (Kato and Ueda 2019; Sato et al. 2009). These earthquakes are a testament to how susceptible life is to displacements along these fault zones and highlight the need to identify zones prone to strong crustal movement in a quest to minimize the effects of destructive earthquakes. Such zones include fault zones which are difficult to ascertain from surficial evidence, as well as active and new fault systems, which are likely to be the locus of future events.

Data and methods

We utilized the vertical component of continuously recorded seismic waveforms by permanent and temporary stations from April 1 to September 30 during the year 2019. The permanent stations included 78 Hi-net stations, 1 Kyushu University station, 1 Tokyo University station, 1 Nagoya University station, 10 AIST stations, 14 Kyoto University stations and 9 JMA stations, and temporary stations comprised 104 Kyoto University Manten project stations (Iio et al. 2018; Katoh et al. 2018), that are distributed around the central part of the Kinki region. We note that velocity type seismometers with the damping constant of 0.7 and the natural frequency of 2 Hz were used for the Manten Project stations. The corresponding poles (p_1 and p_2) and zeros (z_1 and z_2) are $p_1 = -8.7965 - 8.9742i$, $p_2 = -8.7965 + 8.9742i$, $z_1 = z_2 = 0$. Combining these set of stations enabled us to obtain a dataset with adequate short-period surface waves ray paths coverage and a subsequent 3D S-wave velocity

model of high-resolution. Firstly, we computed the cross-correlation of ambient noise to extract surface waves propagating between pairs of seismic stations. We then estimated Rayleigh wave phase velocity measurements between station pairs using the zero-crossing method (Ekström et al. 2009). Finally, we constructed the shallow crustal 3D S-wave velocity structure by applying the direct surface wave inversion method (Fang et al. 2015).

Preprocessing and cross-correlation

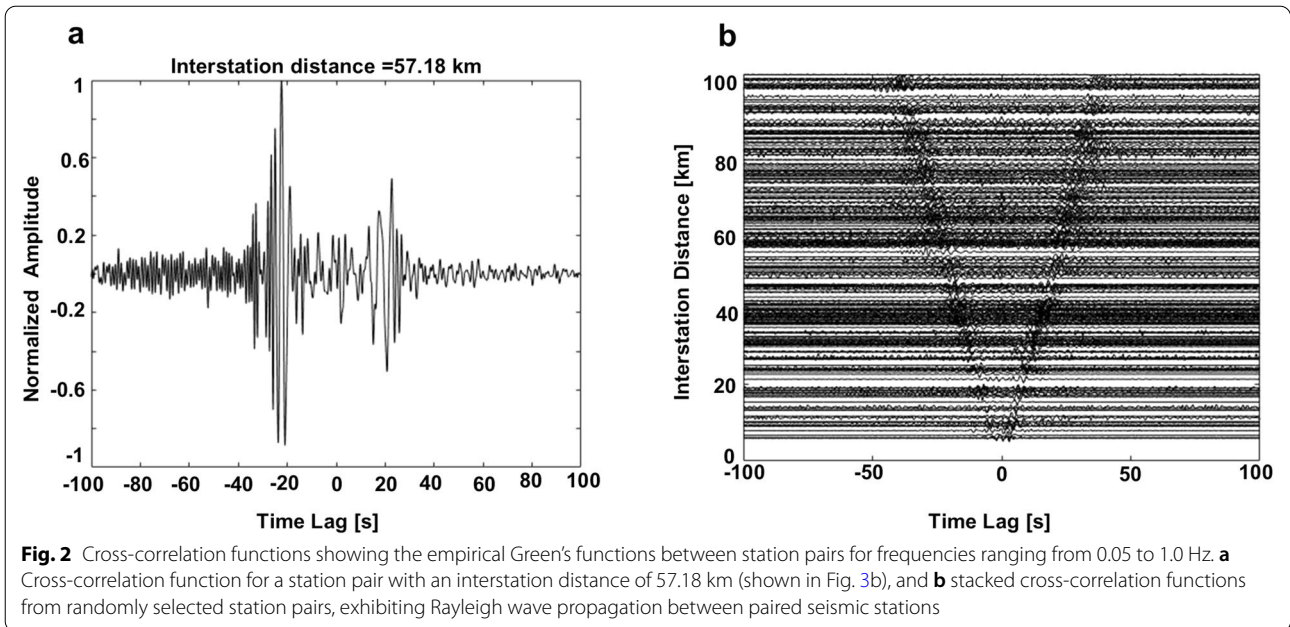
After partitioning daily seismic waveforms into 30-min-long segments with a 50% overlap, we eliminated the instrumental response of each dataset. Next, cross-correlation spectra for all the paired seismic stations were computed from the resulting seismograms (Ekström 2014). Then, the daily cross-correlation spectra were stacked over a 6-month-long time series. The time-domain cross-correlations computed from stacked cross-correlation spectra clearly shows the Rayleigh wave propagation between station pairs (Fig. 2).

Surface wave phase velocity measurements

Phase velocity measurements can be conducted in either the time domain or frequency domain. The time domain analysis requires the high-frequency approximation and only considers those interstation distances exceeding three wavelengths (λ) (Bensen et al. 2007; Lin et al. 2008; Yao et al. 2006). In contrast, the frequency domain approach has no theoretical limitation for interstation distances (i.e., zero-crossing method; Ekström et al. 2009). As such, interstation distances up to approximately one wavelength can be practically used (Ekström et al. 2009; Tsai and Moschetti 2010). In our study, we used the zero-crossing method to derive phase velocity measurements between station pairs. This method is based on modeling cross-correlation spectra by the spatial autocorrelation (SPAC) method (Aki 1957; Asten 2006) and uses the zero-crossing frequencies of the real part of the cross-correlation spectra. The SPAC method is premised on the assumption that ambient noise sources are homogeneously distributed and that ambient noise is predominantly surface waves (Aki 1957). Under this assumption, a Bessel function of the first kind and zeroth order can be used to model the real part of the vertical cross-correlation spectra as follows:

$$\text{Real}(CCS(f, x)) = J_0\left(\frac{2\pi fx}{C_R(f)}\right), \quad (1)$$

where CCS is the cross-spectrum, f is the frequency, x represents the interstation distance, J_0 represents the Bessel function of the first kind and zeroth order, and $C_R(f)$ represents the Rayleigh wave phase velocity. In



the zero-crossing method, we only focus on the zero-crossing points where both sides of Eq. (1) should be zero. The zero-crossing points are not sensitive to fluctuations in the power spectrum of the background noise and non-linear filtering in the data processing (Ekström et al. 2009). Using zero crossings simplifies phase velocity measurements and stabilizes the estimation of phase velocities because phase velocity estimation is not affected by incoherent noise (Cho et al. 2021).

If f_n represents the frequency of the observed n th zero-crossing point of the cross-correlation spectrum, and Z_n denotes the n th zero of the Bessel function, we can match each f_n with the zero-crossing points of the Bessel function to have all the possible phase velocity dispersion curves according to the following equation:

$$C_m(f_n) = \frac{2\pi f_n x}{Z_{n+2m}}, \quad (2)$$

where m representing the number of missed or additional zero-crossing points, takes the values $(0, \pm 1, \pm 2, \dots)$. Applying Eq. (2) for all observed values of f_n yields numerous possible dispersion curves.

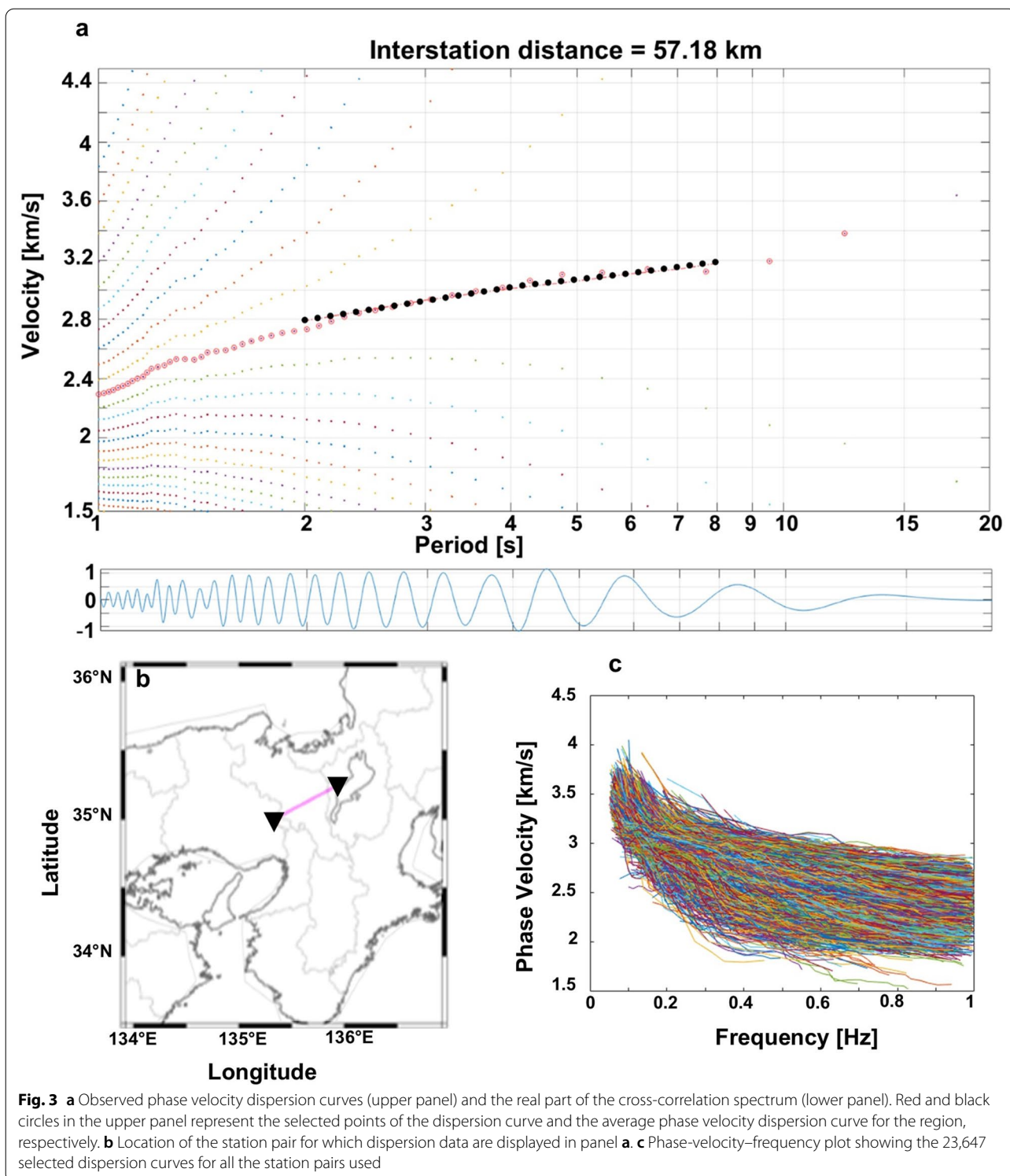
We used the GSpecDisp package (Sadeghisorkhani et al. 2018) to estimate phase velocity dispersion curves uniquely by the zero-crossing method from the stacked cross-correlations. To reduce noise effects in the correlations, we applied a velocity filter of 1–4.5 km/s with a taper interval of ~ 0.2 km/s. Then, we applied spectral whitening to each correlation for amplitude equalization (Sadeghisorkhani et al. 2018). With many possible phase velocities occurring at each frequency with regard

to Eq. (2) (colored dots; Fig. 3a), it is difficult to uniquely determine the phase velocity dispersion curves without using a reference velocity dispersion curve as a guide. To circumvent this, we manually picked the dispersion curve appearing closest to the reference dispersion curve. In the GSpecDisp, average velocities can be estimated by combining all cross-correlation spectra (average velocity module). We estimated average velocities in the period range from 2 to 8 s and used the result as a reference velocity for dispersion curve estimation in single station-pair phase velocity picking mode in GSpecDisp (dashed black dots; Fig. 3a). Finally, we estimated phase velocity dispersion curves between all the possible station pairs (red circles in Fig. 3a).

For our dataset, the maximum measurable period required an interstation distance (x , in km) of at least three wavelengths (λ), defined as the r/λ ratio in GSpecDisp ($x/\lambda \geq 3$). For each cross-correlation function, the signal-to-noise ratio (SNR) was defined as the ratio between maximum absolute amplitude in the signal window (between arrival times corresponding to waves with 1 and 4.5 km/s) and the root mean square amplitude in the noise time window (between 500 and 700 s). We used an SNR threshold of 10 to reject correlations with low signal. Finally, we obtained a total of 23,647 dispersion curves (Fig. 3c).

Direct inversion of the surface wave dispersion curves

Ambient noise tomography using phase velocity dispersion curves typically involves a two-step procedure. Firstly, 2D phase velocity maps are constructed by



travel-time tomography at discrete frequencies. Secondly, pointwise inversion of dispersion data for 1D profiles of S-wave velocity as a function of depth at each grid point is implemented, and combining multiple 1D profiles

subsequently yields the 3D S-wave velocity structure (Shapiro and Ritzwoller 2002; Yao et al. 2008). Nonetheless, a 3D S-wave velocity structure can equally be estimated by direct inversion of dispersion data without the

intermediate step of constructing 2D phase velocity maps (Boschi and Ekström 2002; Feng and An 2010; Pilz et al. 2012). Typically, these direct inversion approaches do not update the ray paths and sensitivity kernels for the newly constructed 3D models.

To estimate the 3D S-wave velocity structure from phase velocity dispersion data, we applied a direct surface wave tomography method (DSurfTomo), which is based on frequency-dependent ray-tracing and a wavelet-based sparsity-constrained inversion (Fang et al. 2015). This approach circumvents the intermediate step of constructing 2D phase velocity maps and iteratively updates the sensitivity kernels of period-dependent dispersion data (Fang et al. 2015). Furthermore, it accounts for the ray-bending effects of period-dependent ray paths by using the fast-marching method (Rawlinson and Sambridge 2004). Accounting for such effects in the inversion is especially useful for short-period surface waves, which are significantly sensitive to the highly complex shallow crustal structure (Fang et al. 2015; Gu et al. 2019). Therefore, this approach is a well-suited tool for determining the shallow-crustal structure of the Kinki region using short-period surface-waves dispersion data.

In tomographic inversion, the objective is to find a model \mathbf{m} that minimizes the differences $\delta t_i(f)$ between the measured travel times $t_i^{obs}(f)$ and the calculated travel times $t_i(f)$ from the model for all frequencies f . The travel time for path i is given as

$$\delta t_i(f) = t_i^{obs}(f) - t_i(f) \approx - \sum_{k=1}^K v_{ik} \frac{\delta C_k(f)}{C_k^2(f)}, \quad (3)$$

where $t_i(f)$ represents the computed travel times from a reference model which can be updated during the inversion, v_{ik} denotes the bilinear interpolation coefficients along the ray path associated with the i th travel-time data, $C_k(f)$ is the phase velocity and its perturbation $\delta C_k(f)$ at the k th two-dimensional surface grid node at frequency f (Fang et al. 2015). Surface wave dispersion is primarily sensitive to S-wave velocity. However, short-period Rayleigh wave dispersion is also sensitive to the compressional (P-wave) velocity in the shallow crustal structure (Fang et al. 2015). The P-wave velocity perturbations together with mass density are therefore explicitly included in the calculation of surface wave dispersion using empirical relationships given by Brocher (2005), with R'_α and R'_ρ as scaling factors, leading to the following equation:

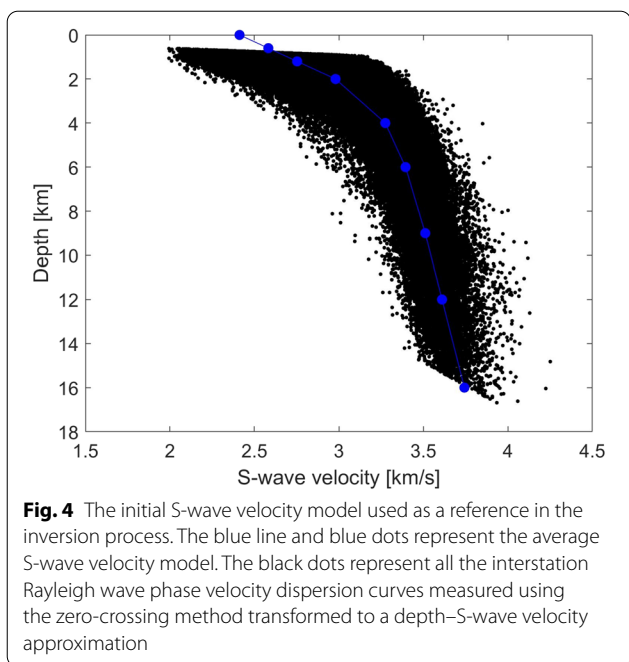
$$\delta t_i(f) = \sum_{k=1}^K \left(-\frac{v_{ik}}{C_k^2} \right) \sum_{j=1}^J \left[R'_\alpha(z_j) \frac{\partial C_k}{\partial \alpha_k(z_j)} + R'_\rho(z_j) \frac{\partial C_k}{\partial \rho_k(z_j)} + \frac{\partial C_k}{\partial \beta_k(z_j)} \right] \Big|_{\theta_k} \delta \beta_k(z_j) = \sum_{l=1}^M G_{il} m_l, \quad (4)$$

where θ_k denotes the one-dimensional (1D) reference model at the k th surface grid node, $\alpha_k(z_j)$, $\rho_k(z_j)$, and $\beta_k(z_j)$ represent the P-wave velocity, the mass density, and the S-wave velocity, respectively. J indicates the number of grid points in the depth direction, and $M = KJ$ represents a sum of all the model grid points. Equation (4) can be written as follows:

$$\mathbf{d} = \mathbf{Gm}, \quad (5)$$

where \mathbf{d} , \mathbf{G} , and \mathbf{m} represent the surface wave travel-time residual vector for all ray paths and discrete frequencies, data sensitivity matrix, and the model parameter vector, respectively. The damping and weighting parameters were applied to balance data fitting and smoothing regularization. These inversion parameters were selected on a trial-and-error basis for our data considering the diverse patterns in inverted S-wave velocity models (weakly smoothed and strongly smoothed S-wave velocity models are shown in Additional file 1: Figures S1 and S2, respectively).

We conducted two inversions with coarser and finer grid intervals between grid points in each horizontal direction for the entire Kinki region and the northern part of the Kinki region (with dense distribution of seismic stations), respectively. The entire Kinki region was parameterized into 53 by 58 grid points on the horizontal plane with 0.055° intervals between grid points in each horizontal direction, whereas the northern part was parameterized into 27 by 75 grid points on the horizontal plane with 0.025° grid point intervals in the latitude and longitude directions. For both inversions, we used 9 grid points along the depth direction (i.e., 0, 0.6, 1.2, 2, 4, 6, 9, 12 and 16 km) and used dispersion data within a frequency bandwidth of 0.0714–1.0 Hz. Empirically, the fundamental mode Rayleigh wave phase velocity is primarily sensitive to $1.1 \times S$ -wave velocity at a depth of about $1/3$ multiplied by its corresponding wavelength (λ) (Fang et al. 2015; Foti et al. 2014; Hayashi 2008). Consequently, we averaged the observed Rayleigh wave phase velocities at depths of about $1/3\lambda$ and then multiplied them by 1.1 to construct the initial S-wave velocity model of the study area (i.e., a one-third wavelength transformation; Fig. 4). To account for the influence of topography on our S-wave velocity models, we subtracted altitude value from the depth value at each grid point. Elevation values were smoothed by applying a moving 2D average smoothing filter with a window size of 18 km by 18 km before correcting for topographic effects. The depth

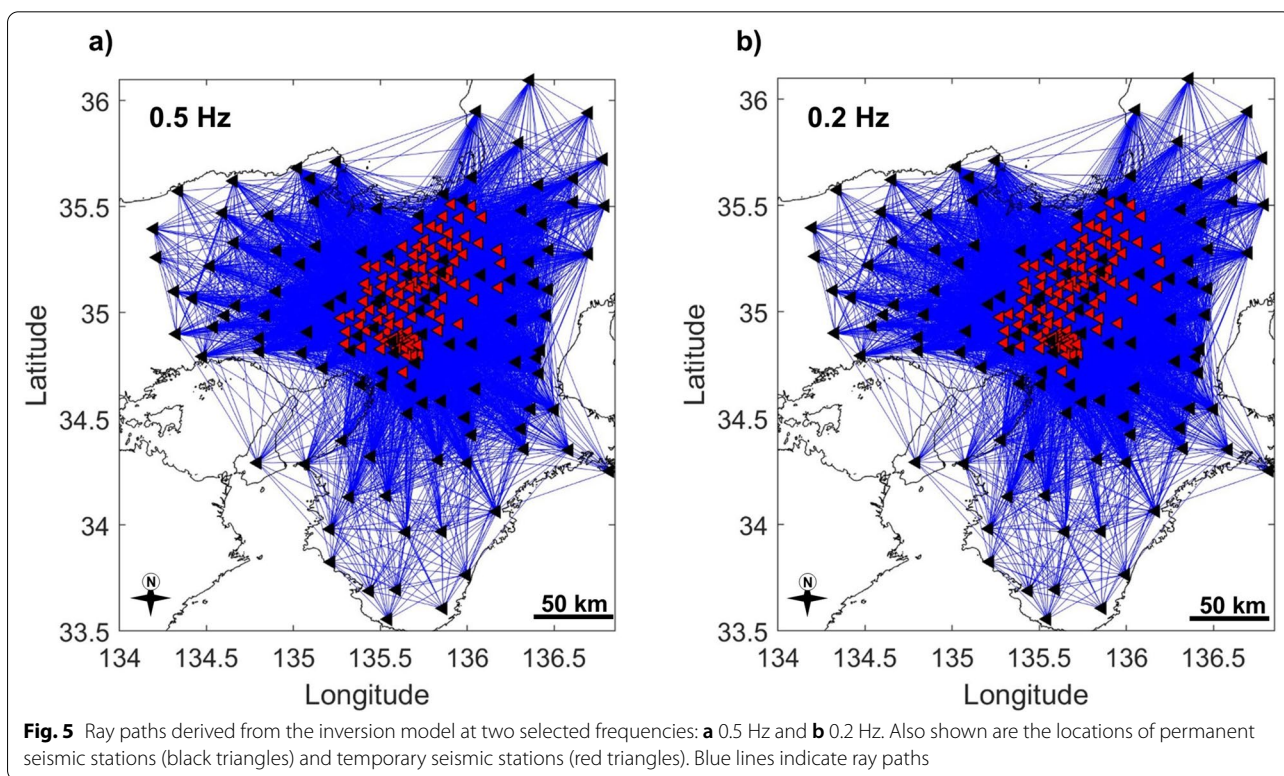


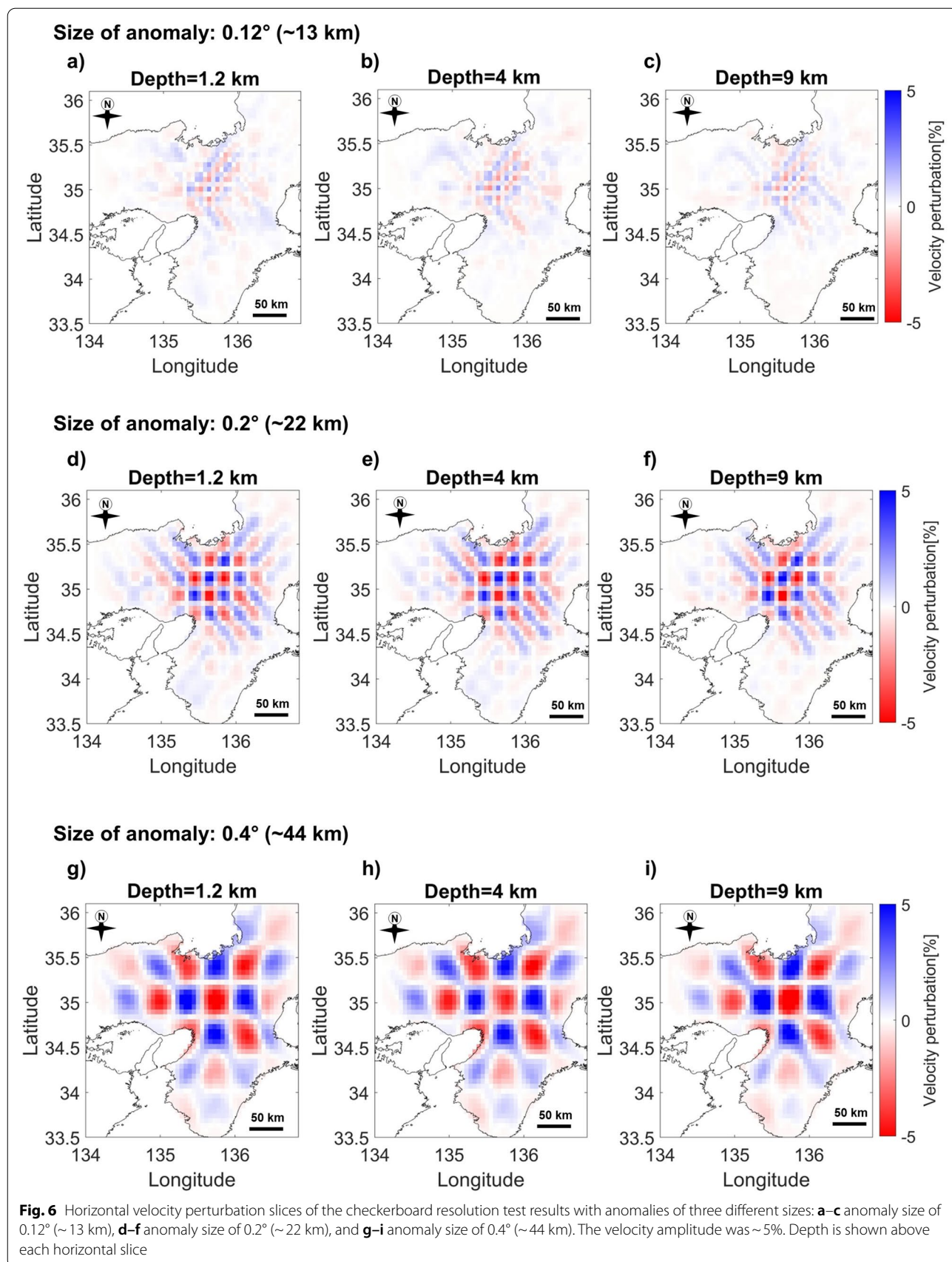
shown in our final 3D S-wave velocity models is the depth below sea level (S-wave velocity models without topographic correction are shown in Additional file 1: Figures S3, S4, S5 and S6).

Results

To construct a 3D S-wave velocity structure of the Kinki region, we applied the direct surface wave tomographic inversion using Rayleigh wave dispersion curves. After inverting the dispersion data, we ensured reliability of our measurements by plotting the spatial ray paths coverage in the study area (Fig. 5). From Fig. 5, it is apparent that the ray paths density is sufficient to resolve small-scale geological features, especially in the most central part of the study area where seismic stations are densely distributed. At the edges, however, the ray paths coverage is slightly limited. We further corroborated reliability of our S-wave velocity model by conducting a checkerboard resolution test using anomalies of 0.12° (~ 13 km; Fig. 6a–c), 0.2° (~ 22 km; Fig. 6d–f) and 0.4° (~ 44 km; Fig. 6g–i) for the entire Kinki region, with an amplitude of the velocity anomaly set to $\sim 5\%$. The checkerboard resolution test (Fig. 6a–c) revealed that tectonic and geological features of ~ 13 km could be well resolved in the central part of the study area where temporary stations are densely distributed, and anomalies of ~ 22 km (Fig. 6d–f) could be observed in most parts of the study area. The anomalies of ~ 44 km (Fig. 6g–i) could be resolved across the entire Kinki region including edge of the study area.

Figure 7 displays selected horizontal slices (map views) at different depths, exhibiting the lateral distribution of S-wave velocities within the study area. The third





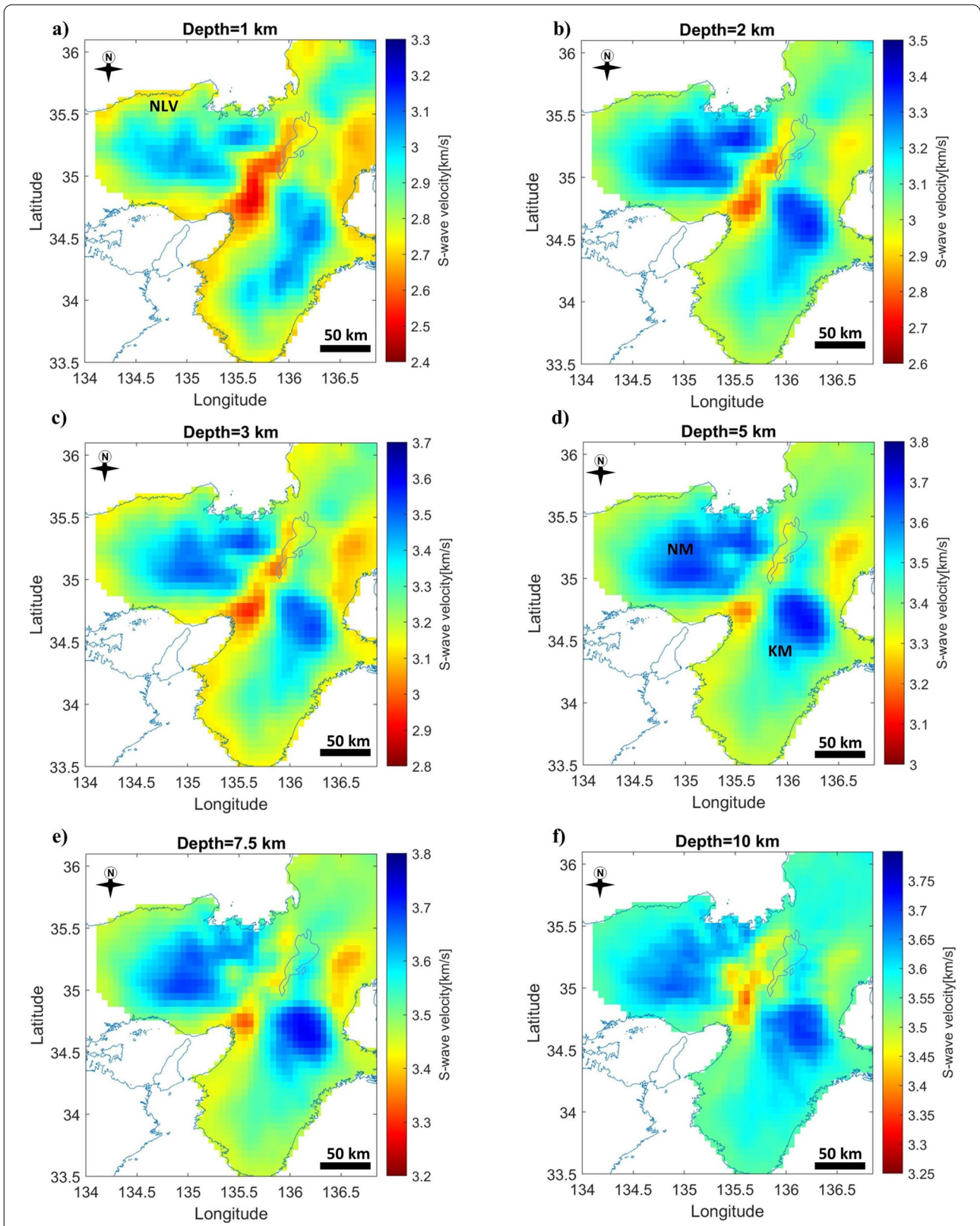
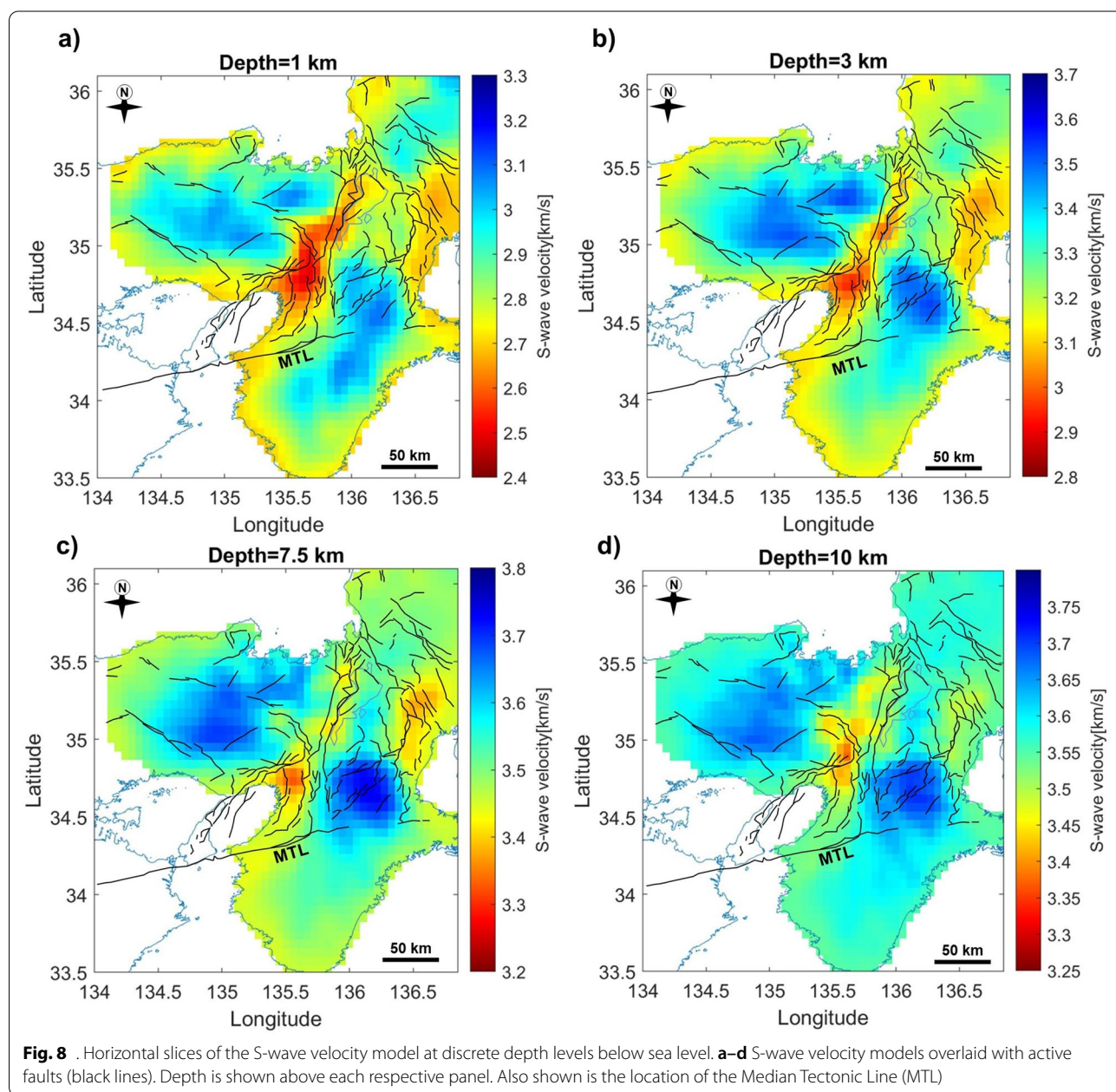


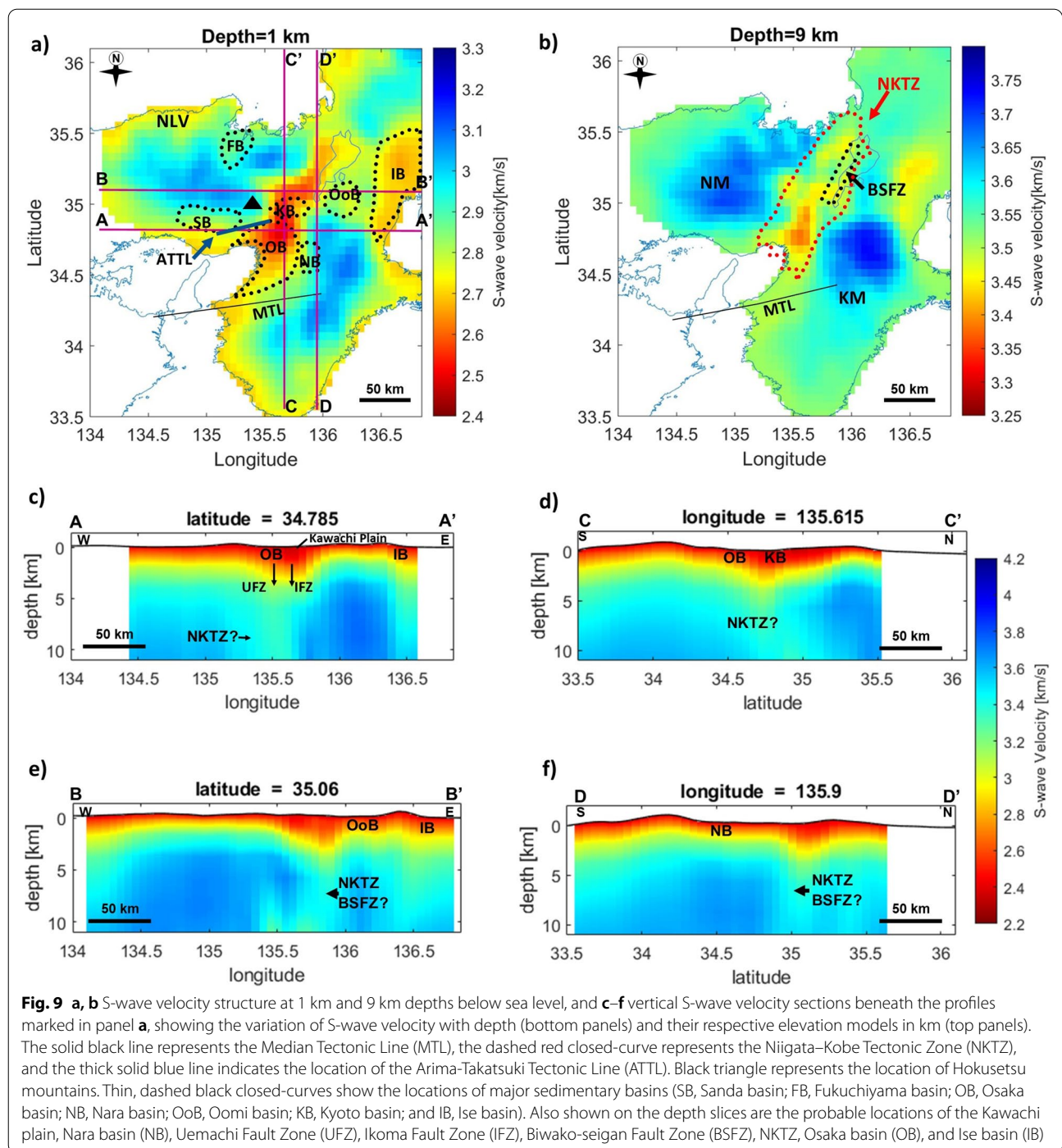
Fig. 7 Horizontal slices of the S-wave velocity model at discrete depth levels below sea level. Depth is shown above each respective panel. **a-f** S-wave velocity models without showing the active faults (S-wave velocity models before correcting for the effects of topography are shown in Figure S4). NM and KM represent the prominent high-velocity anomalies

dimension (depth, in km) is given in the numerical form above each horizontal slice. Significant S-wave velocity heterogeneities are apparent and are discussed in the following sections. These anomalies highlight tectonic and geologic features associated with the study area.

Two broad high-velocity anomalies can be observed in the displayed horizontal slices. The first anomaly (marked NM in Fig. 7d) appears to be trending in the NE–SW direction, whereas the second high-velocity anomaly (marked KM in Fig. 7d) occurs from the southern side of the study area, trending roughly NE–SW across the

MTL. These anomalies agree with the results of Nishida et al. (2008), which indicated comparable S-wave velocities in those areas, particularly at a depth of about 2 km (see Fig. 20 in Nishida et al. 2008). Between the two distinct high-velocity zones exhibited in Nishida et al. (2008), an elongated low-velocity anomaly is evident. Likewise, a prominent low-velocity anomaly is apparent in our results (Figs. 7, 8, 9), flanked on both sides by high-velocity zones (NM and KM) and trending roughly NE–SW. Although our results and those of Nishida et al. (2008) at a depth of about 2 km are similar, our results





show prevalent small-scale (~13 km) low-velocity features at a depth of about 2 km and shallower. In the work of Nishida et al. (2008), the S-wave velocity model is constrained to a minimum depth of about 2 km and such narrow low-velocity zones could not be revealed clearly. The higher lateral resolution of our velocity model at shallow depths (≤ 2 km) than Nishida et al. (2008) model

ascribes to the use of shorter wavelength surface waves and the dense seismic array, particularly in the most central part of the study area where temporary stations (red triangles in Figs. 1b and 5) are densely distributed. Most importantly, prominent anomalies identified in our results correlate well with known geologic features,

including fault zones, sedimentary basins, and mountain ranges.

Interpretations

The high S-wave velocity features observed in the north-western part of the Kinki region (marked NM in Figs. 7d and 9b) are attributable to the presence of the Yakuno intrusive rocks and the Mino/Tamba belts (Fig. 1a). The Yakuno intrusive rocks constitute the Maizuru zone, and the Mino/Tamba belts are Jurassic accretionary complexes composed of non-marine sediments, and the extensively distributed granite batholith (Matsushita 1963; Nakae 1993; Nakajima 1994). Moderate–low ray paths coverage towards the edges of the study area compromises the resolution of our S-wave velocity model. However, the extensive low-velocity anomaly labeled NLV in Fig. 7a is attributable to the Neogene volcanic and sedimentary series of the Tango-Tajima terrain (Matsushita 1963). The high velocities on the southeastern side of the study area may be indicating the presence of the zonally arranged Paleozoic and fossiliferous Mesozoic of the Chichibu terrain, and the scanty fossils along with the undivided Mesozoic of the Hidaka terrain on the southern side of the MTL and the granitic rocks of the Ryoke terrain to the northern side of the MTL (Fig. 1a).

A prominent elongated NE–SW trending low-velocity anomaly occurring between the high-velocity anomalies denoted by NM and KM (Figs. 7f and 9b) is observed. This low-velocity feature is consistent with the location of the Niigata–Kobe Tectonic Zone (NKTZ, Fig. 1a) and the Biwako-seigan Fault Zone on the western shoreline of Lake Biwa (BSFZ; Figs. 9b and 11a). The BSFZ is constituted of the NNE–SSW-trending west-dipping faults separated by clear small gaps or steps (e.g., the Zeze, Hiei, Katata, Hira, Katsuno, Kamidera, Aibano, and Chinai faults; Fig. 11a), and is reported to have a reverse fault sense of east side subsidence (Takemura et al. 2013).

Both the western and eastern sides of the NKTZ are characterized by conspicuous fault systems, with some major faults running through geological units, such as the Yagi-Yabu faults (YGF–YBF) and the Mitoke Fault (MTF) (Mogi et al. 1991). The intervening spaces between fault pairs such as the YGF–YBF and MTF faults are often situated in the terrace and alluvial plain (Katsura 1990). In our results, the low-velocity anomaly observed between the YGF–YBF and the MTF (Fig. 11) probably represent sedimentary units within and around the Fukuchiyama basin (FB), but may also be indicating a possibility of the existence of active faults interconnecting these fault pairs.

Distinct low-velocity anomalies occur at the Sanda basin (SB), FB, Osaka basin (OB), Nara basin (NB), Kyoto

basin (KB), Oomi basin (OoB), and the Ise basin (IB) (Fig. 9). The OB manifest as a near-elliptical low-velocity zone, with the northern and southern edges of this zone appearing to be oriented ENE–WSW and NE–SW, respectively. The low-velocity values in this area are likely to be representing the Plio-Pleistocene Osaka Group sediments (Itihara et al. 1997). The ENE–WSW trending northern boundary of the OB coincides with the location of the Arima-Takatsuki Tectonic Line (ATTL; blue line in Fig. 9a), which is nearly parallel to the MTL (Mitchell et al. 2011). Based on this notion, the ATTL marks the boundary between high-velocity zones (mountainous regions; e.g., the Hokusetsu Mountains) and low-velocity zones (basins; e.g., the SB and OB in Fig. 9a).

According to Hallo et al. (2019), the OB is bounded by two near-parallel reverse faults on its eastern margin, the Uemachi Fault Zone (UFZ) and the Ikoma Fault Zone (IFZ). However, the effect of these fault zones is not clear in our results. Even so, our results reveal a low-velocity feature stretching to deeper parts of the displayed vertical sections (Fig. 9c) occurring between known locations of the UFZ and IFZ. This low-velocity anomaly corresponds to a sub-basin of the OB between the elevated areas of Ikoma and Uemachi Upland (Fig. 9c), designated the Kawachi plain (Hatayama et al. 1995). The high-velocity basement material exhibits undulating topographic pattern, with some synclinal parts representing depressional areas in which deep sedimentary basins occur and anticlinal parts corresponding to the basement upheavals or mountain ranges (Figs. 9c–f and 10c–d). Since surface wave inversion is significantly sensitive to the presence of sediments, the low-velocity anomalies observed at depressional areas are postulated to be representing the prevailing thick sediments (Miyamura et al. 1981; Nakayama 1996; Takemura 1985). At the Ise basin (IB, Fig. 9e), the high-velocity material appears to have subsided significantly. This subsidence may be reflecting the effects of the Kuwana and the Yokkaichi reverse faults, which form part of the nearly N–S trending Yoro fault system (Research Group for Active Faults of Japan 1991). Similar discontinuities within the high-velocity material are evident beneath the OB and KB low-velocity material (Fig. 9c–f), likely to be representing the effects of the NKTZ and/or BSFZ.

To assess the seismic activity correlating to the distribution of anomalous zones identified in this study, we superimposed earthquake hypocenters for the period 2001–2012 (Yano et al. 2017) on the S-wave velocity model (Figs. 10a and 11b). Numerous earthquake hypocenters are observed across the high-velocity zone on the western side of Hira mountain (Mt. Hira in Fig. 11b). By contrast, aligned hypocenter clusters are evident within the NE–SW trending low-velocity zone

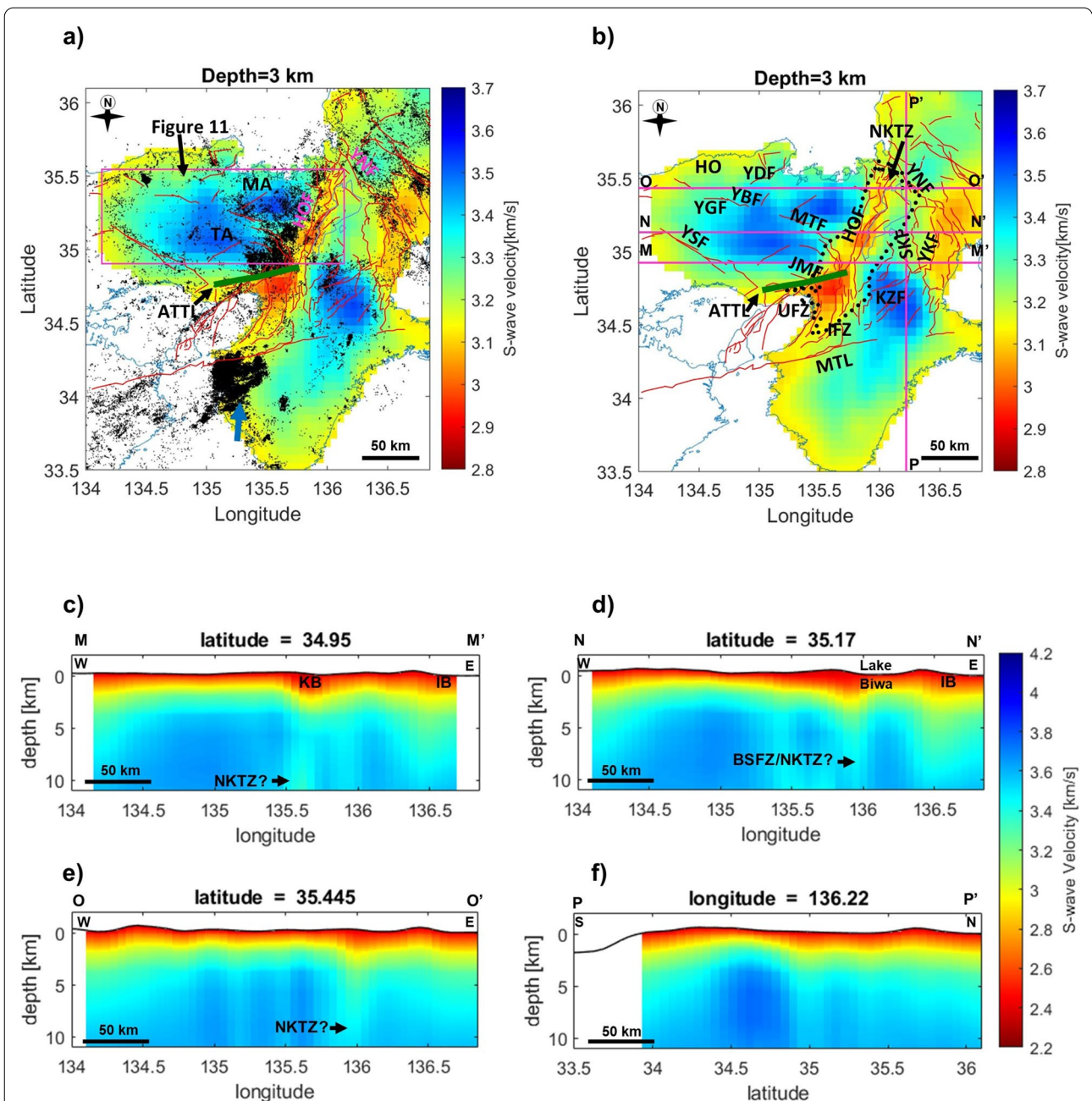


Fig. 10 **a** Map of seismic events that occurred during the January 2001 to December 2012 period (Yano et al. 2017) superimposed on the S-wave velocity model horizontal slice at 3 km depth below sea level. Plotted hypocenters (black dots) are for earthquakes ranging from 0 to 6.5 in moment magnitude for depths shallower than 12 km. Blue arrow indicates the location of dense distribution of earthquake hypocenters along the western part of the Kii Mountainland. **b** Distribution of active faults superimposed on the S-wave velocity model horizontal slice at 3 km depth below sea level. Solid red lines represent active faults documented before this study (Research Group for Active Faults of Japan 1991). Thick dashed black closed-curve and a solid green line indicate the locations of the Niigata–Kobe Tectonic Zone (NKTZ) and the Arima-Takatsuki Tectonic Line (ATTL), respectively. Also shown are the locations of the Median Tectonic Line (MTL), Yamada Fault (YDF), Yamasaki Fault (YSF), Jumantsuji Fault (JMF, a member of the ATTL), Yabu Fault (YBF), Yagi Fault (YGF), Mitoke Fault (MTF), Hanaori Fault (HOF), Kizugawa Fault (KZF), Suzuka Fault (SKF), Yokkaichi Fault (YKF), Yanagase Fault (YNF), Uemachi Fault Zone (UFZ), Ikoma Fault Zone (IFZ), Tanba Block (TA), Hokutan Block (HO), and the Maizuru Block (MA). **c–f** Vertical sections showing the S-wave velocity variation beneath the profiles marked as solid magenta lines in **b**. Inferred locations of the Kyoto basin (KB), Ise basin (IB), Lake Biwa and the Biwako-seigan Fault Zone (BSFZ) and/or Niigata–Kobe Tectonic Line (NKTZ) along the profile are also shown on the vertical sections

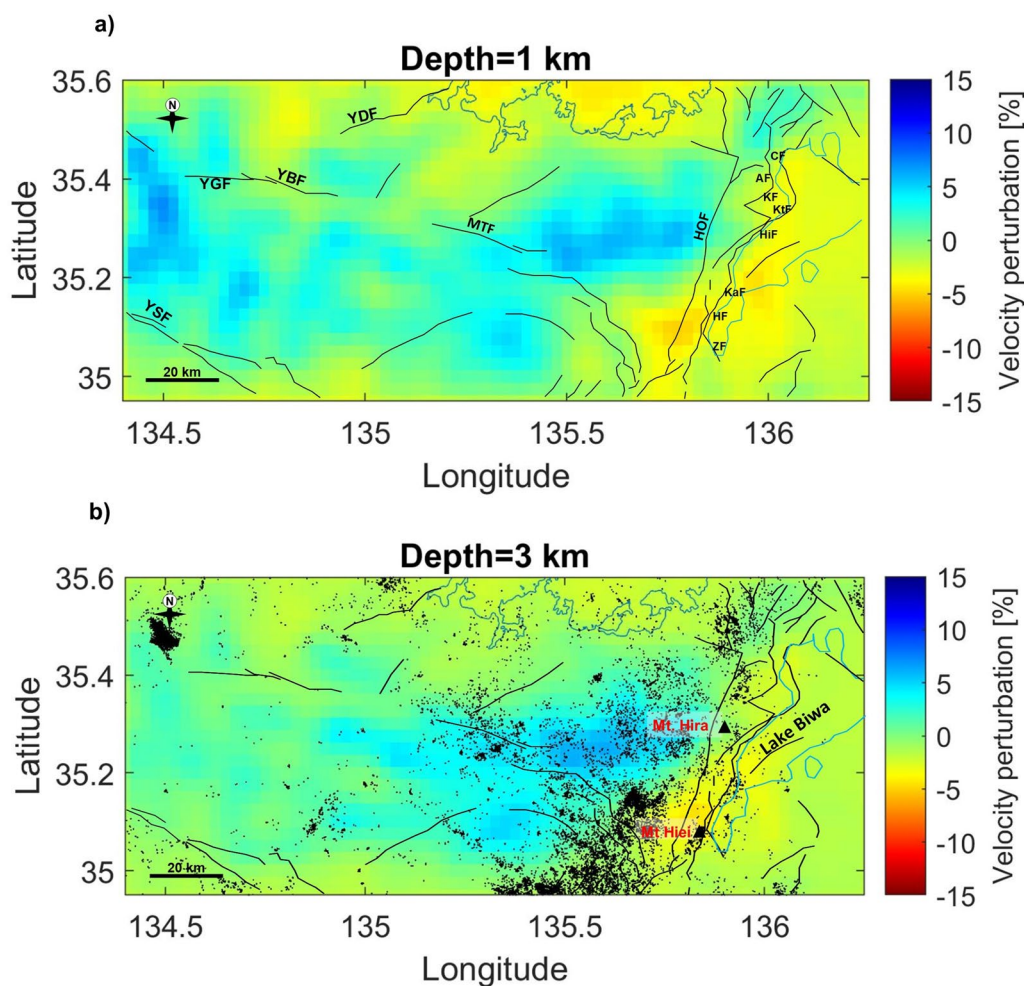


Fig. 11 **a** Enlarged view of the northern part of the Kinki region (shown in Fig. 9) showing the perturbation of S-wave velocity at a depth of 1 km below sea level. Also shown are the locations of the Yamada Fault (YDF), Yamasaki Fault (YSF), Yagi-Yabu Fault (YGF-YBF), Mitoke Fault (MTF), Hanaore Fault (HOF) and the Biwako-seigan Fault Zone members (Chinai Fault, CF; Aibano Fault, AF; Kamidera Fault, KF; Katsuno Fault, KtF; Hira Fault, HIF; Katata Fault, KaF; Hiei Fault, HF; Zeze Fault, ZF) (Kaneda et al. 2008). **b** perturbation of S-wave velocity at a depth of 3 km below sea level, overlaid with earthquake hypocenters (black dots; Yano et al. 2017) and active faults. Black triangles represent the Hira and Hiei mountains. Solid black lines show the location of documented active faults (Research Group for Active Faults of Japan 1991)

consistent with the location of the NKTZ (Fig. 10a). Besides these notable clusters, the northwestern part of the Kinki region has a wide distribution of hypocenters, some of which are aligned in the same trend as elongated low-velocity zones or along the low- and high-velocity zones interface (Figs. 10a and 11b). Some of the linear low-velocity zones that do not coincide with known active fault locations but exhibiting chains of earthquake hypocenters (Fig. 11b) may be representing the weathering effects and sediments associated with the activity of undocumented faults or fault zones.

The low-velocity zone along the western part of the Kii Mountainland (blue arrow in (Fig. 10a) show a dense

distribution of earthquake hypocenters. These conspicuous seismic events are bounded to the north by the MTL and occur mainly within the Sambagawa and Chichibu metamorphic belts. The driving mechanisms of this seismic cluster have been discussed from different point of views in other studies (e.g., Kato et al. 2014; Maeda et al. 2021). In particular, Kato et al. (2014) attribute the observed low-velocity anomaly and a low Poisson's ratio to the presence of fluid-filled cracks, with fluids such as water or partial melt being the key factors driving the increased seismicity; whereas, Maeda et al. (2021) posit that the dense seismic events are likely to be controlled by lithological properties of the crust, and Kanamori

and Tsumura (1971) associate the increased seismicity observed on this low-velocity zone with the regional structural heterogeneities due to the past activity of the MTL.

Conclusions

We used data continuously recorded by a dense seismic array consisting of 221 permanent and temporary seismic stations to estimate a high-resolution shallow 3D *S*-wave velocity model of the Kinki region. *S*-wave phase velocity measurements between station pairs were derived using the zero-crossing method in the frequency domain. We then applied a direct surface wave tomographic inversion using high-frequency ambient noise data (0.0714–1.0 Hz). Our results revealed that *S*-wave velocities vary significantly in the vertical and horizontal directions, which is consistent with the geological heterogeneities of the Kinki region. We attribute the conspicuous high-velocity zones identified in the northwestern and southeastern parts of the study area to the shallow basement material, mountainous regions, or sedimentary complexes. Sedimentary basins manifest as low-velocity zones. Using horizontal and depth slices of the *S*-wave velocity model, we estimated the locations of the recently reactivated Niigata–Kobe Tectonic Zone and the highly active Arima–Takatsuki Tectonic Line on the northern boundary of the Osaka basin. Also, our results clearly reveal the effects of the active Biwako–seigan Fault Zone on the western coast of Lake Biwa (Fig. 8e–f).

We also identified several fine-scale low-velocity tectonic structures, coexisting with known active faults, such as the N–S-, ENE–WSW-, and NE–SW-trending active faults on the eastern side of the Niigata–Kobe Tectonic Zone. Our results revealed elongated low-velocity features that are not consistent with known active faults, likely to be indicating a possible existence of unidentified faults on the northwestern side of the Kinki region (Fig. 11). These findings allude to the improved resolution of our *S*-wave velocity model compared with previous studies of the Kinki region. The observed linear low-velocity zones characterized by aligned distribution of earthquake hypocenters will be useful for hazard assessment and disaster mitigation. The alternating pattern of subsided and uplifted zones observed in the vertical slices of our *S*-wave velocity model is consistent with the tectonic history of the Kinki triangle, which has been dominated by the E–W compressional movement and has numerous active faults of diverse orientations. These results improve our understanding of shallow crustal structure in the Kinki region. Furthermore, a good correlation between heterogeneities in the *S*-wave velocity model and the spatial distribution of fault traces and other geologic features in the Kinki region suggests that

the approach adopted in this study can be utilized as an effective method for unraveling the complex crustal structure of environments akin to the Kinki region.

Abbreviations

AF: Aibano Fault; AIST: National Institute of Advanced Industrial Science and Technology; ANT: Ambient noise tomography; ATTL: Arima–Takatsuki Tectonic Line; BSFZ: Biwako–seigan Fault Zone; CF: Chinai Fault; CT: Chichibu terrain; EUR: Eurasian; FB: Fukuchiyama basin; HF: Hiei Fault; HIF: Hira Fault; HO: Hokutan Block; HOF: Hanaore Fault; HT: Hidaka terrain; IB: Ise basin; IFZ: Ikoma Fault Zone; JMA: Japan Meteorological Agency; Kaf: Katata Fault; KB: Kyoto basin; KF: Kamidera Fault; KtF: Katsuno Fault; KZF: Kizugawa Fault; MA: Maizuru Block; MT: Muro terrain; MTF: Mitoke Fault; MTL: Median Tectonic Line; MZ: Maizuru Zone; NB: Nara basin; NIED: National Research Institute for Earth Science and Disaster Resilience; NKTZ: Niigata–Kobe Tectonic Zone; OB: Osaka basin; OoB: Oomi basin; PHS: Philippine Sea; RAFZ: Rokko Active Fault Zone; RT: Ryoike terrain; SB: Sanda basin; SPAC: Spatial autocorrelation; SKF: Suzuka Fault; SMZ: Sambagawa metamorphic terrain; TA: Tanba Block; TTT: Tango–Tajima terrain; UFZ: Uemachi Fault Zone; YBF: Yabu Fault; YDF: Yamada Fault; YGF: Yagi Fault; YKF: Yokkaichi Fault; YNF: Yanagase Fault; YSF: Yamasaki Fault; ZF: Zeze Fault.

Supplementary Information

The online version contains supplementary material available at <https://doi.org/10.1186/s40623-022-01654-x>.

Additional file 1: Figure S1. Weakly smoothed *S*-wave velocity models with topography correction. This figure is relevant to Figure 7, but the smoothing parameter in velocity inversion is weaker. (a–f) *S*-wave velocity models overlaid with active faults (black lines). **Figure S2.** Strongly smoothed *S*-wave velocity models with topography correction. This figure is relevant to Figure 7, but the smoothing parameter in velocity inversion is stronger. (a–f) *S*-wave velocity models overlaid with active faults (black lines). **Figure S3.** Weakly smoothed *S*-wave velocity models without topographic correction. This figure is relevant to Figure S1. (a–f) *S*-wave velocity models overlaid with active faults (black lines). **Figure S4.** Moderately smoothed *S*-wave velocity models without topographic correction. This figure is relevant to Fig. 7. (a–f) *S*-wave velocity models overlaid with active faults (black lines). **Figure S5.** Strongly smoothed *S*-wave velocity models without topographic correction. This figure is relevant to Figure S2. (a–f) *S*-wave velocity models overlaid with active faults (black lines). **Figure S6.** *S*-wave velocity perturbation of the northern part of the Kinki region without topographic correction. (a) *S*-wave velocity perturbation at a depth of 1 km below sea level. Also shown are the locations of the Yamada Fault (YDF), Yamasaki Fault (YSF), Yagi–Yabu Fault (YGF–YBF), Mitoke Fault (MTF), Hanaore Fault (HOF) and the Biwako–seigan Fault Zone members (Chinai Fault, CF; Aibano Fault, AF; Kamidera Fault, KF; Katsuno, KtF; Hira Fault, HIF; Katata, Kaf; Hiei Fault, HF; Zeze Fault, ZF). (b) *S*-wave velocity perturbation at a depth of 3 km below sea level. Solid black lines represent documented active faults.

Acknowledgements

Seismic data were obtained from the National Research Institute for Earth Science and Disaster Resilience (NIED), the National Institute of Advanced Industrial Science and Technology, the Japan Meteorological Agency, the Disaster Prevention Research Institute of Kyoto University, University of Tokyo, Nagoya University, and Kyushu University. We used a GSpecDisp 1.4 free software package to obtain phase velocity dispersion measurements, which is made available by Sadeghisorkhani et al. (2018) on this website: (<https://github.com/Hamzeh-Sadeghi/GSpecDisp>). We utilized a surface wave inversion program to directly invert our dispersion data (DSurfTomo; Fang et al. 2015), which is available from (<https://github.com/HongjianFang/DSurfTomo> Version 1.3). For data analysis and visualization we used a MATLAB R2020b program. The computations in this work were partly performed using the computer facilities at the Research Institute for Information Technology, Kyushu University. This work was supported by Japan Society for the Promotion of Science (JSPS) KAKENHI (Grant Numbers JP19K23544, JP20K04133, and JP20H01997).

Author contributions

BN analyzed the data and drafted the initial manuscript. TT proposed this study. TI, HN, TT suggested the method for data processing and analysis, and revised the manuscript. YI acquired continuous seismic data in and around the Kinki region, and revised the manuscript. All authors contributed significantly to data analysis and interpretation of the results. All authors reviewed and approved the final manuscript.

Funding

This work was supported by Japan Society for the Promotion of Science (JSPS) KAKENHI (Grant Numbers JP19K23544, JP20K04133, JP20H01997, and JP21H05202).

Availability of data and materials

Continuous seismic waveform data from the Hi-net stations can be obtained from the NIED website (<http://www.bosai.go.jp/er/>). Continuous seismic data from the Kyushu University station, Tokyo University station, Nagoya University stations, AIST stations, Kyoto University stations, JMA stations and Kyoto University Manten project stations are available on request. The dispersion data used to produce Fig. 3c can be accessed at (<https://doi.org/10.6084/m9.figshare.17989979>). Our S-wave velocity data are available from this URL (<https://doi.org/10.6084/m9.figshare.17138672>, Licence CC BY 4.0). Earthquake hypocenters used superimposed on our S-wave velocity models was published by the Japan Unified hi-resolution relocated Catalog for Earthquakes (JUICE) project, and can be accessed at this website (https://www.hinet.bosai.go.jp/topics/JUICE/3d/Juice_Hypo3D_Kinki_2001-2012.html; Yano et al. 2017).

Declarations

Competing interests

The authors declare that they have no competing interests.

Author details

¹Department of Earth Resources Engineering, Kyushu University, 744 Motoooka, Nishi-ku, Fukuoka 819-0395, Japan. ²Earth and Environmental Sciences Department, Botswana International University of Science and Technology, P/Bag 16, Palapye, Botswana. ³International Institute for Carbon-Neutral Energy Research (WPI-I2CNER), Kyushu University, 744 Motoooka, Nishi-ku, Fukuoka 819-0395, Japan. ⁴Geological Survey of Japan, National Institute of Advanced Industrial Science and Technology (AIST), Ibaraki 305-8567, Japan. ⁵Department of Systems Innovation, Faculty of Engineering, The University of Tokyo, Tokyo 113-8656, Japan. ⁶Disaster Prevention Research Institute, Kyoto University, Kyoto 611-0011, Japan.

Received: 25 January 2022 Accepted: 31 May 2022

Published online: 20 June 2022

References

- Aki K (1957) Space and time spectra of stationary stochastic waves, with special reference to microtremors. *Bull Earth Res Ins* 35:415–456
- Aoki S, Iio Y, Katao H et al (2016) Three-dimensional distribution of S wave reflectors in the northern Kinki district, southwestern Japan. *Earth Planets Space* 68:1–9. <https://doi.org/10.1186/s40623-016-0468-3>
- Asten MW (2006) On bias and noise in passive seismic data from finite circular array data processed using SPAC methods. *Geophysics* 71:V153–V162. <https://doi.org/10.1190/1.2345054>
- Barnes GL (2008) The making of the Japan Sea and the Japanese Mountains: understanding Japan's volcanism in structural context. *Jpn Rev* 20:3–52
- Bensen GD, Ritzwoller MH, Barmin MP et al (2007) Processing seismic ambient noise data to obtain reliable broad-band surface wave dispersion measurements. *Geophys J Int* 169:1239–1260. <https://doi.org/10.1111/j.1365-246X.2007.03374.x>
- Boschi L, Ekström G (2002) New images of the Earth's upper mantle from measurements of surface wave phase velocity anomalies. *J Geophys Res Solid Earth* 107:1–20. <https://doi.org/10.1029/2000JB000059>
- Brocher TM (2005) Empirical relations between elastic wavespeeds and density in the Earth's crust. *Bull Seism Soc Am* 95:2081–2092. <https://doi.org/10.1785/0120050077>
- Chen KX, Gung Y, Kuo BY, Huang TY (2018) Crustal magmatism and deformation fabrics in northeast Japan revealed by ambient noise tomography. *J Geophys Res Solid Earth* 123:8891–8906. <https://doi.org/10.1029/2017JB015209>
- Cho I, Senna S, Wakai A et al (2021) Basic performance of a spatial autocorrelation method for determining phase velocities of Rayleigh waves from microtremors, with special reference to the zero-crossing method for quick surveys with mobile seismic arrays. *Geophys J Int* 226:1676–1694. <https://doi.org/10.1093/gji/ggab149>
- Ekström G (2014) Love and Rayleigh phase-velocity maps, 5–40 s, of the western and central USA from USArray data. *Earth Planet Sci Lett* 402:42–49. <https://doi.org/10.1016/j.epsl.2013.11.022>
- Ekström G, Abers GA, Webb SC (2009) Determination of surface-wave phase velocities across USArray from noise and Aki's spectral formulation. *Geophys Res Lett* 36:5–9. <https://doi.org/10.1029/2009GL039131>
- Fang H, Yao H, Zhang H et al (2015) Direct inversion of surface wave dispersion for three-dimensional shallow crustal structure based on ray tracing: methodology and application. *Geophys J Int* 201:1251–1263. <https://doi.org/10.1093/gji/ggv080>
- Feng M, An M (2010) Lithospheric structure of the Chinese mainland determined from joint inversion of regional and teleseismic Rayleigh-wave group velocities. *J Geophys Res Solid Earth* 115:1–16. <https://doi.org/10.1029/2008JB005787>
- Foti S, Lai CG, Rix GJ, Strobbia C (2014) Surface wave methods for near-surface site characterization. CRC Press, Taylor & Francis Group LLC
- GSJ-AIST (2021) Geological survey of Japan, AIST. <https://gbank.gsj.jp/subsurface/english/ondemand.php>. Accessed 19 Nov 2021
- Gu N, Wang K, Gao J et al (2019) Shallow crustal structure of the Tanlu Fault Zone near Chao Lake in eastern China by direct surface wave tomography from local dense array ambient noise analysis. *Pure Appl Geophys* 176:1193–1206. <https://doi.org/10.1007/s00024-018-2041-4>
- Hallo M, Opršal I, Asano K, Gallovič F (2019) Seismotectonics of the 2018 northern Osaka M6. 1 earthquake and its aftershocks: joint movements on strike-slip and reverse faults in inland Japan. *Earth Planets Space* 71:1–21. <https://doi.org/10.1186/s40623-019-1016-8>
- Hatayama K, Matsunami K, Iwata T, Irikura K (1995) Basin-induced Love waves in the eastern part of the Osaka basin. *J Phys Earth* 43:131–155. <https://doi.org/10.4294/jpe1952.43.131>
- Hayashi K (2008) Development of surface-wave methods and its application to site investigations, (Doctoral dissertation). Retrieved from Kyoto University Research Information Repository. (<http://hdl.handle.net/2433/57255>). Japan: Kyoto University.
- Huzita K (1980) Role of the Median Tectonic Line in the Quaternary tectonics of the Japanese Islands. *Mem Geol Soc Japan* 18:129–153
- Hyodo M, Hirahara K (2003) A viscoelastic model of interseismic strain concentration in Niigata-Kobe Tectonic Zone of central Japan. *Earth Planets Space* 55:667–675. <https://doi.org/10.1186/BF03352473>
- Iio Y (1996) A possible generating process of the 1995 southern Hyogo Prefecture earthquake: stick of fault and slip on detachment. *Jishin* 49:103–112. https://doi.org/10.4294/zisin1948.49.1_103
- Iio Y, Kishimoto S, Nakao S et al (2018) Extremely weak fault planes: an estimate of focal mechanisms from stationary seismic activity in the San'in district, Japan. *Tectonophysics* 723:136–148. <https://doi.org/10.1016/j.tecto.2017.12.007>
- Itihara M, Yoshikawa S, Kamei T (1997) 24 The Pliocene-Pleistocene boundary in Japan: the Osaka Group. *Pleistocene Bound Begin Quat* 41:239. <https://doi.org/10.1017/CBO9780511585760.026>
- Ito K, Umeda Y, Sato H et al (2006) Deep seismic surveys in the Kinki district: Shingu-Maizuru line. *Bull Earthquake Res Inst Univ Tokyo* 81:239–245
- Kanamori H (1995) The Kobe (Hyogo-ken Nanbu), Japan, earthquake of January 16, 1995. *Seismol Res Lett* 66:6–10. <https://doi.org/10.1785/gssrl.66.2.6>
- Kanamori H, Tsumura K (1971) Spatial distribution of earthquakes in the Kii peninsula, Japan, south of the Median Tectonic Line. *Tectonophysics* 12:327–342. [https://doi.org/10.1016/0040-1951\(71\)90020-5](https://doi.org/10.1016/0040-1951(71)90020-5)
- Kaneda H, Kinoshita H, Komatsubara T (2008) An 18,000-year record of recurrent folding inferred from sediment slices and cores across a blind segment of the Biwako-seigan fault zone, central Japan. *J Geophys Res Solid Earth* 113:1–19. <https://doi.org/10.1029/2007JB005300>
- Katao H, Maeda N, Hiramatsu Y et al (1997) Detailed mapping of focal mechanisms in/around the 1995 Hyogo-ken Nanbu earthquake rupture zone. *J Phys Earth* 45:105–119. <https://doi.org/10.4294/jpe1952.45.105>

- Kato A, Ueda T (2019) Source fault model of the 2018 M w 5.6 northern Osaka earthquake, Japan, inferred from the aftershock sequence. *Earth Planets Space* 71:1–9. <https://doi.org/10.1186/s40623-019-0995-9>
- Kato A, Kurashimo E, Igarashi T et al (2009) Reactivation of ancient rift systems triggers devastating intraplate earthquakes. *Geophys Res Lett* 36:L05301. <https://doi.org/10.1029/2008GL036450>
- Kato A, Saiga A, Takeda T et al (2014) Non-volcanic seismic swarm and fluid transportation driven by subduction of the Philippine Sea slab beneath the Kii Peninsula, Japan. *Earth Planet Space* 66:1–8. <https://doi.org/10.1186/1880-5981-66-86>
- Kato A, Sakai S, Matsumoto S et al (2021) Conjugate faulting and structural complexity on the young fault system associated with the 2000 Tottori earthquake. *Commun Earth Environ* 2:1–9. <https://doi.org/10.1038/s43247-020-00086-3>
- Katoh S, Iio Y, Katao H et al (2018) The relationship between S-wave reflectors and deep low-frequency earthquakes in the northern Kinki district, southwestern Japan. *Earth Planets Space* 70:1–11. <https://doi.org/10.1186/s40623-018-0921-6>
- Katsura I (1990) Block structure bounded by active strike-slip faults in the northern part of Kinki district, southwest Japan. *Mem Fac Sci Kyoto Univ Ser Geol Mineral* 55:57–123. Retrieved from Kyoto University Research Information Repository. <http://hdl.handle.net/2433/186665>
- Lin FC, Moschetti MP, Ritzwoller MH (2008) Surface wave tomography of the western United States from ambient seismic noise: Rayleigh and Love wave phase velocity maps. *Geophys J Int* 173:281–298. <https://doi.org/10.1111/j.1365-246X.2008.03720.x>
- Maeda S, Toda S, Matsuzawa T et al (2021) Influence of crustal lithology and the thermal state on microseismicity in the Wakayama region, southern Honshu, Japan. *Earth Planets Space* 73:1–10. <https://doi.org/10.1186/s40623-021-01503-3>
- Matsubara M, Obara K, Kasahara K (2008) Three-dimensional P- and S-wave velocity structures beneath the Japan Islands obtained by high-density seismic stations by seismic tomography. *Tectonophysics* 454:86–103. <https://doi.org/10.1016/j.tecto.2008.04.016>
- Matsushita R, Imanishi K (2015) Stress fields in and around metropolitan Osaka, Japan, deduced from microearthquake focal mechanisms. *Tectonophysics* 642:46–57. <https://doi.org/10.1016/j.tecto.2014.12.011>
- Matsushita S (1963) Geological history of the Kinki District, Japan during the Cainozoic Era (Preliminary note). Special Contributions of the Geophysical Institute, Kyoto University 2:113–124. Retrieved from Kyoto University Research Information Repository. <http://hdl.handle.net/2433/178442>
- Mitchell TM, Ben-Zion Y, Shimamoto T (2011) Pulverized fault rocks and damage asymmetry along the Arima-Takatsuki Tectonic Line, Japan. *Earth Planet Sci Lett* 308:284–297. <https://doi.org/10.1016/j.epsl.2011.04.023>
- Miyamura M, Yoshida F, Yamada N et al (1981) Geology of the Kameyama district: Quadrangle Series. Geological Survey of Japan 128.
- Mogi T, Katsura I, Nishimura S (1991) Magnetotelluric survey of an active fault system in the northern part of Kinki District, southwest Japan. *J Struct Geol* 13:235–240. [https://doi.org/10.1016/0191-8141\(91\)90070-Y](https://doi.org/10.1016/0191-8141(91)90070-Y)
- Nakae S (1993) Jurassic accretionary complex of the Tamba Terrane, Southwest Japan, and its formative process. *J Geosci Osaka City Univ* 36:15–70
- Nakajima T (1994) The Ryoke plutonometamorphic belt: crustal section of the Cretaceous Eurasian continental margin. *Lithos* 33:51–66. [https://doi.org/10.1016/0024-4937\(94\)90053-1](https://doi.org/10.1016/0024-4937(94)90053-1)
- Nakajima J, Hirose F, Hasegawa A (2009) Seismotectonics beneath the Tokyo metropolitan area, Japan: effect of slab-slab contact and overlap on seismicity. *J Geophys Res Solid Earth* 114:1–23. <https://doi.org/10.1029/2008JB006101>
- Nakayama K (1996) Depositional models for fluvial sediments in an intra-arc basin: an example from the Upper Cenozoic Tokai Group in Japan. *Sediment Geol* 101:193–211. [https://doi.org/10.1016/0037-0738\(95\)00065-8](https://doi.org/10.1016/0037-0738(95)00065-8)
- Nimiya H, Ikeda T, Tsuji T (2020) Three-dimensional s wave velocity structure of Central Japan estimated by surface-wave tomography using ambient noise. *J Geophys Res Solid Earth* 125:1–18. <https://doi.org/10.1029/2019JB019043>
- Nishida K, Kawakatsu H, Obara K (2008) Three-dimensional crustal S wave velocity structure in Japan using microseismic data recorded by Hi-net tiltmeters. *J Geophys Res Solid Earth* 113:1–22. <https://doi.org/10.1029/2007JB005395>
- Obara K, Kasahara K, Hori S, Okada Y (2005) A densely distributed high-sensitivity seismograph network in Japan: Hi-net by National Research Institute for Earth Science and Disaster Prevention. *Rev Sci Instrum* 76:021301. <https://doi.org/10.1063/1.1854197>
- Oike K (1976) Spatial and temporal distribution of micro-earthquakes and active faults. *Mem Geol Soc Japan* 12:59–73
- Pilz M, Parolai S, Picozzi M, Bindi D (2012) Three-dimensional shear wave velocity imaging by ambient seismic noise tomography. *Geophys J Int* 189:501–512. <https://doi.org/10.1111/j.1365-246X.2011.05340.x>
- Rawlinson N, Sambridge M (2004) Wave front evolution in strongly heterogeneous layered media using the fast marching method. *Geophys J Int* 156:631–647. <https://doi.org/10.1111/j.1365-246X.2004.02153.x>
- Research Group for Active Faults of Japan (1991) Active faults in Japan: sheet maps and inventories. University of Tokyo press, p 437
- Sabra KG, Gerstoft P, Roux P (2005) Surface wave tomography from micro-seisms in Southern California. *Geophys Res Lett* 32:1–4. <https://doi.org/10.1029/2005gl023155>
- Sadeghisorkhani H, Gudmundsson Ó, Tryggvason A (2018) GSpecDisp: a matlab GUI package for phase-velocity dispersion measurements from ambient-noise correlations. *Comput Geosci* 110:41–53. <https://doi.org/10.1016/j.cageo.2017.09.006>
- Sagiya T, Miyazaki SI, Tada T (2000) Continuous GPS array and present-day crustal deformation of Japan. *Pure Appl Geophys* 157:2303–2322. <https://doi.org/10.1007/PL00022507>
- Sato H, Ito K, Abe S et al (2009) Deep seismic reflection profiling across active reverse faults in the Kinki Triangle, central Japan. *Tectonophysics* 472:86–94. <https://doi.org/10.1016/j.tecto.2008.06.014>
- Shapiro NM, Ritzwoller MH (2002) Monte-Carlo inversion for a global shear-velocity model of the crust and upper mantle. *Geophys J Int* 151:88–105. <https://doi.org/10.1046/j.1365-246X.2002.01742.x>
- Shapiro NM, Campillo M, Stehly L, Ritzwoller MH (2005) High-resolution surface-wave tomography from ambient seismic noise. *Science* 307:1615–1618. <https://doi.org/10.1126/science.1108339>
- Suemoto Y, Ikeda T, Tsuji T, Iio Y (2020) Identification of a nascent tectonic boundary in the San-in area, southwest Japan, using a 3D S-wave velocity structure obtained by ambient noise surface wave tomography. *Earth Planets Space* 72:1–13. <https://doi.org/10.1186/s40623-020-1139-y>
- Taira A (2001) Tectonic evolution of the Japanese island arc system. *Annu Rev Earth Planet Sci* 29:109–134. <https://doi.org/10.1146/annurev.earth.29.1.109>
- Takemura K, Haraguchi T, Kusumoto S, Itoh Y (2013) Tectonic basin formation in and around Lake Biwa, Central Japan. *Mechan Sedim Basin Form* 9:209–229. <https://doi.org/10.5772/56667>
- Takemura K (1985) The Plio-Pleistocene Tokai Group and the tectonic development around Ise Bay of central Japan since Pliocene. *Mem Fac Sci Kyoto Univ Ser Geol Mineral* 51:21–96. Retrieved from Kyoto University Research Information Repository. <http://hdl.handle.net/2433/186655>
- Tsai VC, Moschetti MP (2010) An explicit relationship between time-domain noise correlation and spatial autocorrelation (SPAC) results. *Geophys J Int* 182:454–460. <https://doi.org/10.1111/j.1365-246X.2010.04633.x>
- Usami T (2003) Materials for comprehensive list of destructive earthquakes in Japan. Univ. of Tokyo Press, Tokyo, p 605
- Wakita K (2013) Geology and tectonics of Japanese islands: a review—the key to understanding the geology of Asia. *J Asian Earth Sci* 72:75–87. <https://doi.org/10.1016/j.jseaes.2012.04.014>
- Weaver RL, Lobkis OI (2004) Diffuse fields in open systems and the emergence of the Green's function (L). *J Acoust Soc Am* 116:2731–2734. <https://doi.org/10.1121/1.1810232>
- Yang Y (2014) Application of teleseismic long-period surface waves from ambient noise in regional surface wave tomography: a case study in western USA. *Geophys J Int* 198:1644–1652. <https://doi.org/10.1093/gji/ggu234>
- Yano TE, Takeda T, Matsubara M, Shiomi K (2017) Japan unified high-resolution relocated catalog for earthquakes (JUICE): crustal seismicity beneath the Japanese Islands. *Tectonophysics* 702:19–28. <https://doi.org/10.1016/j.tecto.2017.02.017>
- Yao H, van Der Hilst RD, De Hoop MV (2006) Surface-wave array tomography in SE Tibet from ambient seismic noise and two-station analysis—I. Phase velocity maps. *Geophys J Int* 166:732–744. <https://doi.org/10.1111/j.1365-246X.2006.03028.x>
- Yao H, Beghein C, Van Der Hilst RD (2008) Surface wave array tomography in SE Tibet from ambient seismic noise and two-station analysis-II. Crustal

and upper-mantle structure. *Geophys J Int* 173:205–219. <https://doi.org/10.1111/j.1365-246X.2007.03696.x>

Yolsal-Cevikbilen S, Biryol CB, Beck S et al (2012) 3-D crustal structure along the North Anatolian Fault Zone in north-central Anatolia revealed by local earthquake tomography. *Geophys J Int* 188:819–849. <https://doi.org/10.1111/j.1365-246X.2011.05313.x>

Publisher's Note

Springer Nature remains neutral with regard to jurisdictional claims in published maps and institutional affiliations.

Submit your manuscript to a SpringerOpen[®] journal and benefit from:

- ▶ Convenient online submission
- ▶ Rigorous peer review
- ▶ Open access: articles freely available online
- ▶ High visibility within the field
- ▶ Retaining the copyright to your article

Submit your next manuscript at ▶ [springeropen.com](https://www.springeropen.com)
